

Scaling laws for the cutoff wavenumber of the short-wavelength ion-temperature-gradient mode in a Z-pinch

O. Gupta^{1,2†}, M. Barnes^{1,3}, F. I. Parra⁴, L. Podavini⁵, A. Zocco⁵, T. Adkins⁴ and P. G. Ivanov⁶

¹Rudolf Peierls Centre for Theoretical Physics, University of Oxford, Oxford OX1 3PU, UK

²Mathematical Institute, University of Oxford, OX2 6GG, UK

³University College, Oxford OX1 4BH, UK

⁴Princeton Plasma Physics Laboratory, Princeton, NJ 08540, USA

⁵Max-Planck-Institut für Plasmaphysik, 17491 Greifswald, Germany

⁶United Kingdom Atomic Energy Authority, Culham Campus, Abingdon, OX14 3DB, UK

(Received xx; revised xx; accepted xx)

We use a heuristic fluid model to predict the dependence of the cutoff wave number for the short-wavelength ion temperature gradient (SWITG) mode on ion density gradient, ion temperature gradient (ITG) and ion-electron temperature ratio. In particular, we predict that the cutoff wave number increases linearly with increasing ITG for sufficiently large values of the ITG. Direct numerical solutions of the gyrokinetic dispersion relation using a purpose-built solver confirm the predicted scalings at large ITG values and find a weaker power-law scaling for intermediate ITG values. Combining these wave number scalings with a simple diffusive estimate for turbulent fluxes produces a scaling prediction for the ITG heat flux in SWITG-driven turbulence. Applying the critical balance conjecture additionally provides scalings for the aspect ratio of the SWITG turbulent eddies.

1. Introduction

Turbulent transport driven by small-scale instabilities is known to limit the energy confinement time in tokamaks (Yoshida *et al.* 2025) and optimised stellarators (Bozhenkov *et al.* 2020). Though there is a plethora of such instabilities, each catalogued by the ingredients required, the archetypal instability for ion transport is the curvature-driven ion-temperature-gradient (ITG) instability (Pogutse 1968; Terry *et al.* 1982; Guzdar *et al.* 1983; Romanelli 1989; Evensen *et al.* 1998). It has been the subject of numerous experimental, numerical and analytical studies. While the precise details of the instability depend on the magnetic geometry and the plasma profiles, its key features are a growth rate that increases with increasing ITG beyond a critical value and a characteristic wavelength that is comparable to or larger than the ion Larmor radius.

More recently, it was shown that a short-wavelength version of the ITG instability, referred to as the SWITG mode, exists (Hassam *et al.* 1990; Guo & Romanelli 1993; Smolyakov *et al.* 2002). A key feature of the SWITG identified in previous studies is the appearance of a second maximum in the linear growth rate spectrum at scales smaller than the ion Larmor scale (Pu & Migliuolo 1985; Smolyakov *et al.* 2002; Hirose *et al.* 2002; Gao *et al.* 2003, 2005, 2006; Chowdhury *et al.* 2009, 2012; Jagannath *et al.* 2020; Singh *et al.* 2023; Rodríguez & Zocco 2025). There are both slab and toroidal variants of

† Email address for correspondence: om.gupta@maths.ox.ac.uk

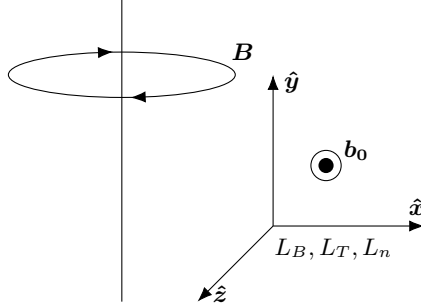


Figure 1: An illustration of the Z-pinch geometry adopted in our analysis. We use orthonormal coordinates (x, y, z) such that a constant curvature magnetic field exists along the \hat{z} direction with all equilibrium gradients taken to be along the \hat{x} direction.

the SWITG, driven by resonances with parallel streaming and binormal magnetic drifts, respectively. The dependence of the SWITG growth rates on various plasma parameters has been explored in some detail in sheared slab and toroidal geometry, with and without electromagnetic effects, and in both local and radially ‘global’ models. A more limited number of nonlinear simulations have also been conducted. Due to the complicated nature of many of the models used for these studies, both the range of parameter space considered and the availability of general analytical results have necessarily been limited.

To complement these full-physics studies, we develop here a minimal model to study the curvature-driven variant of the SWITG mode. This model consists of fluid ions and Boltzmann electrons in a Z-pinch magnetic geometry. The simplicity of our model enables analytical calculation of mode growth rates and facilitates the identification of a simple scaling for the SWITG mode cutoff scale with both the ion density and temperature gradient scale lengths as well as the ion-electron temperature ratio. Our scalings are confirmed via numerical solution of the linear dispersion relation with both a purpose-built dispersion solver and with the gyrokinetic code `stella` (Barnes *et al.* 2019).

The paper is laid out as follows: In Section 2 we describe our model system and state our ordering and other simplifying assumptions, culminating in the linearised gyrokinetic-Poisson equations that we use as the starting point in our analysis. We then develop a heuristic fluid model in Section 3 and evaluate the associated dispersion relation in the long- and short-wavelength limits. Here the main novel result is an expression for the minimum unstable wavenumber for the SWITG as a function of density and temperature gradient scale lengths, as well as the ion-electron temperature ratio. The prediction for this cutoff wavenumber is compared with the exact results from a full gyrokinetic analysis in Section 4. The possible implications of this scaling for turbulence are explored in Section 5, and we conclude with an overview and prospective for future work in Section 6.

2. Electrostatic gyrokinetic model in a Z-pinch

For simplicity, we restrict our attention to a plasma consisting of electrons of charge $-e$ and a single ion species of mass m and charge Ze , immersed in a constant-curvature magnetic field of the form $\mathbf{B} = B(x)\hat{z}$. The equilibrium plasma density n and temperature T are inhomogeneous, with variation only in the x direction. Here (x, y, z) is the set of orthonormal coordinates illustrated in Figure 1, with \hat{z} the unit vector in the z direction. For the case of vanishing magnetic shear considered here, the magnetic

geometry is equivalent to that of a Z-pinch, with x , y and z the radial, axial and azimuthal coordinates, respectively.

We work in the collisionless, electrostatic limit and assume that electron motion along the magnetic field is sufficiently fast that the electron density is well approximated by a Boltzmann response: $\delta n_e = (e\varphi/T_e)n_e$, where δn_e and n_e are the fluctuating and equilibrium components of the electron density, respectively, φ is the electrostatic potential and T_e is the equilibrium electron temperature. Finally, we focus on fluctuations that have no variation along the equilibrium magnetic field: These ‘flute’ perturbations are the most unstable in a constant-curvature system and are the simplest approximation to curvature ITG modes in the bad-curvature region of tokamaks.

2.1. Gyrokinetic model equations

We assume the fluctuations in our plasma satisfy the standard δf -gyrokinetic ordering (Thomas M. Antonsen & Lane 1980; Frieman & Chen 1982; Sugama & Horton 1997; Abel *et al.* 2013); i.e., fluctuations with characteristic frequency ω and wavenumbers k_{\parallel} and k_{\perp} parallel and perpendicular to the direction of the equilibrium magnetic field $\mathbf{b} = \hat{\mathbf{z}}$ are ordered such that

$$\epsilon \equiv \frac{\rho_i}{L} \sim \frac{\omega}{\Omega} \sim \frac{k_{\parallel}}{k_{\perp}} \sim \frac{e\varphi}{T_i} \ll 1, \quad (2.1)$$

where $\Omega = ZeB/mc$ is the ion cyclotron frequency, $\rho_i = v_{\text{th}}/\Omega$ is the thermal ion Larmor radius, $v_{\text{th}} = \sqrt{2T_i/m}$ is the ion thermal speed and L is a typical equilibrium length scale. In addition, it is assumed that all equilibrium quantities evolve on the time scale $\tau_E^{-1} \sim \epsilon^3 \Omega$, so they may be treated as static in the discussion that follows. The fluctuating ion distribution function can then be written to lowest order in ϵ as

$$\delta f = -\frac{Ze\varphi}{T_i} f_0 + h, \quad (2.2)$$

consisting of a Boltzmann part and a gyrokinetic part h that is independent of gyro-phase angle at fixed guiding centre position $\mathbf{R} = \mathbf{r} - \mathbf{b} \times \mathbf{v}/\Omega$, with \mathbf{r} and \mathbf{v} the particle position and velocity, respectively. To lowest order in ϵ , the equilibrium distribution function f_0 is a Maxwellian,

$$f_0 = \frac{n_i}{\pi^{3/2} v_{\text{th}}^3} e^{-v^2/v_{\text{th}}^2}, \quad (2.3)$$

with $n_i = n_i(x)$ the equilibrium ion density and $v_{\text{th}} = v_{\text{th}}(x)$.

The resultant (electrostatic, two-dimensional) gyrokinetic evolution equation for h is

$$\frac{\partial}{\partial t} \left(h - \frac{Ze\langle\varphi\rangle_{\mathbf{R}}}{T_i} f_0 \right) + \mathbf{v}_d \cdot \nabla_{\perp} h + \mathbf{v}_{\varphi} \cdot \nabla_{\perp} (h + f_0) = 0, \quad (2.4)$$

where $\langle \dots \rangle_{\mathbf{R}}$ denotes a gyro-average at constant guiding centre position and \mathbf{v}_{φ} and \mathbf{v}_d are the (gyro-averaged) $E \times B$ and magnetic drift velocities, respectively. In an arbitrary geometry with vanishing plasma beta they are given by

$$\mathbf{v}_{\varphi} = \frac{c}{B} \mathbf{b} \times \nabla \langle \varphi \rangle_{\mathbf{R}}, \quad \mathbf{v}_d = \frac{\mathbf{b}}{\Omega} \times \nabla \ln B \left(v_{\parallel}^2 + \frac{v_{\perp}^2}{2} \right), \quad (2.5)$$

with v_{\parallel} and v_{\perp} the components of \mathbf{v} along and across \mathbf{b} , respectively.

The gyrokinetic system is closed by enforcing quasineutrality,

$$\delta n_e = Z\delta n_i = Z \int d^3 \mathbf{v} \left(-\frac{Ze\varphi}{T_i} n_i + \int d^3 \mathbf{v} \langle h \rangle_{\mathbf{r}} \right), \quad (2.6)$$

where $\langle \dots \rangle_{\mathbf{r}}$ denotes an average over gyro-angle at fixed \mathbf{r} . Upon application of the Boltzmann electron assumption, (2.6) can be rearranged to provide an explicit equation for φ in terms of h :

$$\frac{e\varphi}{T_e} (1 + \tau^{-1}) n_i = \int d^3 \mathbf{v} \langle h \rangle_{\mathbf{r}}, \quad (2.7)$$

where we have defined $\tau \equiv T_i/ZT_e$.

2.2. Fourier representation

In our linear analysis of (2.4) and (2.7), we will find it convenient to work within a Fourier representation in both space and time. In deriving the gyrokinetic equation (2.4), we have assumed equilibrium quantities and their local gradients can be taken as constant on the space-time scales of the fluctuations. Hence, all coefficients multiplying h and φ in (2.4) and (2.7) are independent of x, y, z and t .

We decompose h and φ in the Fourier series

$$h = \sum_{\mathbf{k}} \hat{h}_{\mathbf{k}} (v_{\parallel}, v_{\perp}, t) e^{i\mathbf{k} \cdot \mathbf{R}}, \quad \varphi = \sum_{\mathbf{k}} \hat{\varphi}_{\mathbf{k}} (t) e^{i\mathbf{k} \cdot \mathbf{r}}. \quad (2.8)$$

Neglecting the nonlinear term in (2.4) and performing a Fourier transform in time results in the linearised gyrokinetic equation for the Fourier coefficient $\hat{h}_{\mathbf{k}}$,

$$\begin{aligned} \omega \left(\hat{h}_{\mathbf{k}} - \frac{J_0(\alpha_k)}{\tau} \frac{e\hat{\varphi}_{\mathbf{k}}}{T_e} f_0 \right) - \omega_d \left(\frac{2v_{\parallel}^2}{v_{\text{th}}^2} + \frac{v_{\perp}^2}{v_{\text{th}}^2} \right) \hat{h}_{\mathbf{k}} \\ + \omega_* \left[1 + \eta \left(\frac{v^2}{v_{\text{th}}^2} - \frac{3}{2} \right) \right] \frac{J_0(\alpha_k)}{\tau} \frac{e\hat{\varphi}_{\mathbf{k}}}{T_e} f_0 = 0, \end{aligned} \quad (2.9)$$

where J_0 is the zeroth-order Bessel function of the first kind, $\alpha_k = k_{\perp} v_{\perp} / \Omega$, $\eta = L_n / L_T$, $L_X^{-1} = -d \ln X / dx$, with X one of B, n or T , and the drift and diamagnetic frequencies are, respectively,

$$\omega_d = -\frac{k_y \rho_i}{2} \frac{v_{\text{th}}}{L_B} \quad \omega_* = -\frac{k_y \rho_i}{2} \frac{v_{\text{th}}}{L_n}. \quad (2.10)$$

To evaluate the gyro-averages in Fourier space, we have made use of the identity (Abramowitz & Stegun 1968)

$$\langle \varphi(\mathbf{r}, t) \rangle_{\mathbf{R}} = \sum_{\mathbf{k}} \hat{\varphi}_{\mathbf{k}} e^{i\mathbf{k} \cdot \mathbf{R}} \frac{1}{2\pi} \oint d\vartheta \exp \left(i \frac{k_{\perp} v_{\perp}}{\Omega} \cos(\vartheta) \right) = \sum_{\mathbf{k}} J_0(\alpha_k) \hat{\varphi}_{\mathbf{k}} e^{i\mathbf{k} \cdot \mathbf{R}}, \quad (2.11)$$

where ϑ is the gyro-angle.

Similarly, the Fourier representation of the quasineutrality condition (2.7) is

$$\frac{e\hat{\varphi}_{\mathbf{k}}}{T_e} (1 + \tau^{-1}) n_i = \int d^3 \mathbf{v} J_0(\alpha_k) \hat{h}_{\mathbf{k}}, \quad (2.12)$$

where

$$\langle h(\mathbf{R}, v_{\perp}, v_{\parallel}, t) \rangle_{\mathbf{r}} = \sum_{\mathbf{k}} \hat{h}_{\mathbf{k}} e^{i\mathbf{k} \cdot \mathbf{r}} \frac{1}{2\pi} \oint d\vartheta \exp \left(-i \frac{k_{\perp} v_{\perp}}{\Omega} \cos(\vartheta) \right) = \sum_{\mathbf{k}} J_0(\alpha_k) \hat{h}_{\mathbf{k}} e^{i\mathbf{k} \cdot \mathbf{r}}. \quad (2.13)$$

Equations (2.9) and (2.12) form a closed system of equations for the Fourier coefficients $\hat{h}_{\mathbf{k}}$ and $\hat{\varphi}_{\mathbf{k}}$.

3. Heuristic fluid model

Before undertaking a direct gyrokinetic analysis, we first construct and examine a heuristic fluid model. We will see that a quantitatively correct treatment of the short-wavelength ITG instability requires retention of resonant effects that are absent from this simple fluid model. Nonetheless, the fluid model captures qualitatively the salient features of the instability and facilitates a comparison with the standard long-wavelength ITG instability, including its stabilisation by a density gradient.

We take as our starting point the gyrokinetic equation (2.9) and the quasineutrality condition (2.12) in Fourier space. Multiplying (2.9) by $J_0(\alpha_k)/n_i$ and integrating over velocity space gives

$$\omega \left[\frac{\delta N_k}{n_i} - \frac{\Gamma_0(b_k)}{\tau} \frac{e\hat{\varphi}_k}{T_e} \right] - \omega_d \frac{\delta p_k}{n_i T_i} + [\Gamma_0(b_k) + \eta b_k (\Gamma_1(b_k) - \Gamma_0(b_k))] \frac{\omega_* e\hat{\varphi}_k}{\tau T_e} = 0, \quad (3.1)$$

where

$$\delta N_k \equiv \int d^3 v J_0(\alpha_k) \hat{h}_k \quad (3.2)$$

is the density deviation from an ion Boltzmann response,

$$\delta p_k \equiv \int d^3 v \frac{m}{2} (2v_{\parallel}^2 + v_{\perp}^2) J_0(\alpha_k) \hat{h}_k \quad (3.3)$$

is a combination of the parallel and perpendicular fluctuating pressures, $b_k = k_{\perp}^2 \rho_i^2 / 2$ and $\Gamma_j(b) = \exp(-b) I_j(b)$, with I_j the j 'th modified Bessel function of the first kind.

We close our fluid model by multiplying (2.9) by $[J_0(\alpha_k)/n_i](2v_{\parallel}^2 + v_{\perp}^2)/v_{\text{th}}^2$, integrating over the velocity space, and neglecting the term proportional to ω_d . This is an *ad hoc* assumption that can be justified if $\omega \gg \omega_d$ or if the moments of h beyond the energy moment are asymptotically small. For long-wavelength ITG modes, the solutions for ω thus obtained satisfy $\omega \gg \omega_d$, while for short-wavelength ITG modes they do not. This will lead us to conduct a full gyrokinetic analysis of the short-wavelength instability in the next section, but we will find that the correct qualitative features of the instability are captured by the fluid approach. The resulting equation for δp_k is

$$\omega \left[\frac{\delta p_k}{n_i T_i} - \frac{K_1(b_k)}{\tau} \frac{e\hat{\varphi}_k}{T_e} \right] + [K_1(b_k) + \eta K_2(b_k)] \frac{\omega_* e\hat{\varphi}_k}{\tau T_e} = 0, \quad (3.4)$$

where K_1 and K_2 are defined to be

$$K_1(b_k) = (2 - b_k) \Gamma_0(b_k) + b_k \Gamma_1(b_k) \quad (3.5)$$

and

$$K_2(b_k) = 2(b_k - 1)^2 \Gamma_0(b_k) + b_k(3 - 2b_k) \Gamma_1(b_k). \quad (3.6)$$

Combining the density equation (3.1), the pressure equation (3.4) and the quasineutrality condition (2.12) results in a quadratic dispersion relation for ω :

$$a_2 \omega^2 + a_1 \omega + a_0 = 0, \quad (3.7)$$

where $a_0 = \omega_d \omega_*(K_1 + \eta K_2)$, $a_1 = -\omega_d K_1 + \omega_* [\Gamma_0 + \eta b_k (\Gamma_1 - \Gamma_0)]$ and $a_2 = \tau + 1 - \Gamma_0$. The solutions for ω are then

$$\omega_{\pm} = -\frac{a_1}{2a_2} \pm \frac{\sqrt{a_1^2 - 4a_0 a_2}}{2a_2}. \quad (3.8)$$

3.1. Long-wavelength limit

Evaluating (3.8) for $L_B/L_T \gg 1$ and $\eta \sim \tau \sim 1$ in the long-wavelength limit $b_k \ll 1$, we obtain

$$\omega_{\pm}^{\text{lw}} \approx -\frac{\omega_*}{2\tau} \pm \frac{\sqrt{\omega_*^2 - 8\omega_*\omega_d\tau(1+\eta)}}{2\tau}, \quad (3.9)$$

where we have used $\Gamma_0(b_k) \approx 1$ and $\Gamma_1(b_k) \approx 0$. When the temperature gradient is much steeper than the density gradient so that $\eta\omega_d\tau \gg \omega_*$, we recover the standard (fluid) growth rate for strongly-driven, long-wavelength curvature-driven ITG modes (Horton *et al.* 1981):

$$\omega_{\pm}^{\text{lw}} \approx \pm ik_y\rho_i \frac{c_s}{\sqrt{L_B L_p}}, \quad (3.10)$$

with $c_s = \sqrt{T_e/m}$ the sound speed and $L_p^{-1} = L_n^{-1} + L_T^{-1}$ the inverse ion pressure gradient scale length. However, if $\eta\omega_d\tau \sim \omega_*$, then the term under the radical in (3.9) can vanish. At this marginal stability point, we find a critical η below which the long-wavelength ITG mode is stabilised:

$$\eta_{\text{crit}} \approx \sqrt{\frac{1}{8\tau} \frac{L_B}{L_T}}. \quad (3.11)$$

Note that for $\eta \sim \eta_{\text{crit}} \gg 1$, the associated frequency is $\omega = -\omega_*/2\tau \gg \omega_d$, consistent with the assumption we used to close our fluid model.

3.2. Short-wavelength limit

Next, we evaluate (3.8) in the short-wavelength limit, for which

$$\Gamma_0(b_k) \approx \frac{1}{\sqrt{\pi}} \frac{1}{k_{\perp}\rho_i} \left(1 + \frac{1}{4} \frac{1}{k_{\perp}^2 \rho_i^2} \right), \quad \Gamma_1(b_k) \approx \frac{1}{\sqrt{\pi}} \frac{1}{k_{\perp}\rho_i} \left(1 - \frac{3}{4} \frac{1}{k_{\perp}^2 \rho_i^2} \right). \quad (3.12)$$

Inserting these expansions into (3.8) and taking $L_B/L_T \gg 1$ gives

$$K_1 \approx \frac{3}{2\sqrt{\pi}} \frac{1}{k_{\perp}\rho_i}, \quad K_2 \approx \frac{3}{4\sqrt{\pi}} \frac{1}{k_{\perp}\rho_i}, \quad (3.13)$$

$$a_0 \approx \omega_d\omega_* (2 + \eta) \frac{3}{4\sqrt{\pi}} \frac{1}{k_{\perp}\rho_i}, \quad (3.14)$$

$$a_1 \approx \frac{1}{2\sqrt{\pi}} \frac{1}{k_{\perp}\rho_i} [(2 - \eta)\omega_* - 3\omega_d], \quad (3.15)$$

and

$$a_2 \approx 1 + \tau - \frac{1}{\sqrt{\pi}} \frac{1}{k_{\perp}\rho_i}. \quad (3.16)$$

For fixed values of η , L_B/L_n and τ , marginal stability occurs at the cutoff wave number k_{\perp}^o , given by

$$k_{\perp}^o \rho_i = \frac{(2 - \eta)^2}{(2 + \eta)} \frac{L_B}{12L_n^{\text{eff}}}, \quad (3.17)$$

where we have defined the effective density gradient scale length $L_n^{\text{eff}} \equiv (1 + \tau)L_n$. Note that for $\eta \rightarrow \infty$, this cutoff wavelength simplifies to $k_{\perp}^o \rho_i = (1/12)(L_B/L_T^{\text{eff}})$, with $L_T^{\text{eff}} \equiv (1 + \tau)L_T$.

4. Linear gyrokinetic analysis

To capture correctly the short-wavelength instability with $\omega \sim \omega_d$, we return to the gyrokinetic system given by Eqs. (2.9) and (2.12). Rearrangement of (2.9) provides an expression for the non-Boltzmann part of the fluctuating distribution function \hat{h}_k :

$$\hat{h}_k = \frac{\omega - \omega_* [1 + \eta (\tilde{v}^2 - 3/2)]}{\omega - \omega_d (2\tilde{v}_\parallel^2 + \tilde{v}_\perp^2)} \frac{J_0(\alpha_k)}{\tau} \frac{e\hat{\varphi}_k}{T_e} f_0, \quad (4.1)$$

where the tildes on the velocity variables indicate normalisation by v_{th} . Substitution of (4.1) into the quasineutrality condition (2.12) results in the dispersion relation

$$1 + \tau = \frac{2}{\sqrt{\pi}} \int_{-\infty}^{\infty} d\tilde{v}_\parallel \int_0^{\infty} d\tilde{v}_\perp \tilde{v}_\perp \frac{\omega - \omega_* [1 + \eta (\tilde{v}^2 - 3/2)]}{\omega - \omega_d (2\tilde{v}_\parallel^2 + \tilde{v}_\perp^2)} e^{-\tilde{v}^2} J_0^2(\alpha_k). \quad (4.2)$$

Our program in this section consists of solving Eq. (4.2) for ω across a range of values for $k_\perp \rho_i$, η , L_B/L_T and τ , with a particular emphasis on the short-wavelength, steep gradient regime. The solutions we obtain are semi-analytical and are facilitated by using a convergent power series expansion for $J_0^2(\alpha_k)$ (Ivanov & Adkins 2023), as described in Appendix A. This approach is computationally efficient: Calculating ω for a single \mathbf{k}_\perp takes less than a second on a single core of a home laptop. Our solutions are also verified against data from linear gyrokinetic simulations obtained using the flux tube gyrokinetic code **stella** (Barnes *et al.* 2019). Unless otherwise specified, all **stella** simulations were run with 48 grid points in parallel velocity and 12 in magnetic moment, with maximum values in both v_\parallel and v_\perp of three times the ion thermal speed.

As there is no radial component of the magnetic drift in a Z-pinch, the wave number k_x appears only via k_\perp when it appears as an argument to various Bessel functions. Although we consider the impact of including k_x at the end of this section, most of our discussion involves setting $k_x = 0$, $k_\perp \equiv k_y$ and analysing 1D spectral plots. We also set $\tau = 1$ unless otherwise specified.

4.1. $\eta \rightarrow \infty$ limit

We first consider the case with no equilibrium density gradient, for which $\eta \rightarrow \infty$. The dependence of the growth rate and real frequency on $k_y \rho_i$ and L_B/L_T for this case is given in Fig. 2. The long-wavelength ITG instability discussed in Section 3.1 is present when $k_y \rho_i \lesssim 1$, and the short-wavelength ITG instability discussed in Section 3.2 is present when $k_y \rho_i \gtrsim 1$. The instability range for these modes overlaps for small enough L_B/L_T , but a gap develops between them as L_B/L_T increases. This is seen more clearly in Fig. 3, where one-dimensional cuts of the growth rate and real frequency are taken at two different values of L_B/L_T (with additional examples provided in Appendix B). As anticipated in Sec. 3.1, the long-wavelength ITG growth rate is linearly proportional to $k_y \rho_i$ for $k_y \rho_i \ll 1$ and is suppressed when $k_y \rho_i \gtrsim 1$. In contrast, the short-wavelength ITG mode requires a minimum k_y for instability, and this minimum value increases with L_B/L_T . This leads to the unusual behaviour of the growth rate decreasing with L_B/L_T over a range of k_y values (1 $\lesssim k_y \rho_i \lesssim 3$ for the L_B/L_T values considered in Fig. 3).

4.2. $\eta \sim 1$ limit

We now consider the addition of an equilibrium density gradient of magnitude comparable to the temperature gradient, i.e., $\eta \sim 1$. The growth rates and real frequencies for a range of $k_y \rho_i$ and L_B/L_T values are plotted in Fig. 4 when $\eta = 1$. As observed in previous studies and anticipated in Sec. 3.1, the long-wavelength ITG mode is eliminated

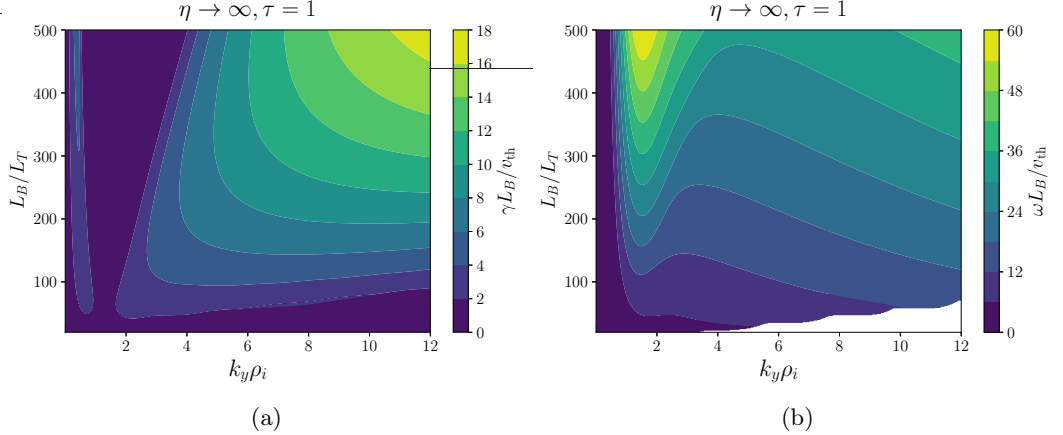


Figure 2: 2-D scan in L_B/L_T and $k_y\rho_i$ of the (a) growth rate and (b) real frequency obtained with the solver for $\tau = 1$ and no density gradient ($\eta \rightarrow \infty$). Note the presence of two distinct peaks in the growth rate spectrum and a non-monotonic frequency spectrum, both key features of the SWITG. The real frequency is not shown in a narrow region at small drive and very short-wavelength where no growing modes exist and it is numerically challenging to calculate.

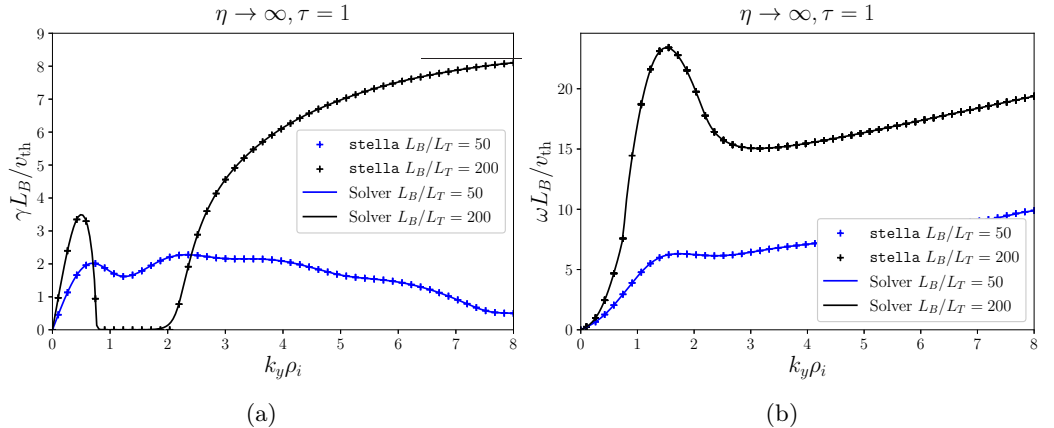


Figure 3: Plots of the (a) growth rate and (b) real frequency spectra for $L_B/L_T = 50$ and 200 with $\tau = 1$ and $\eta \rightarrow \infty$. The growth-rate spectra show both the long-wavelength ITG mode and the short-wavelength SWITG branch driven by FLR effects. Despite the two instability regions, the real frequency remains continuous and always in the ion diamagnetic direction.

for η below some critical value η_{crit} . It is possible to quantify this relation further through a scan of η_{crit} against L_B/L_T , as in Fig. 5 (see Appendix B for additional plots of the growth rate spectra at different η values). We find that the prediction for the critical η given by Eq. (3.11) is a good approximation for the long-wavelength ITG. For $\eta < \eta_{\text{crit}}$ the overall stability of the system is determined by the short-wavelength ITG mode. This is particularly clear in the one-dimensional cuts at two different L_B/L_T values shown in Fig. 6.

It is evident from both Figs. 4 and 6 that there is a minimum wave number required

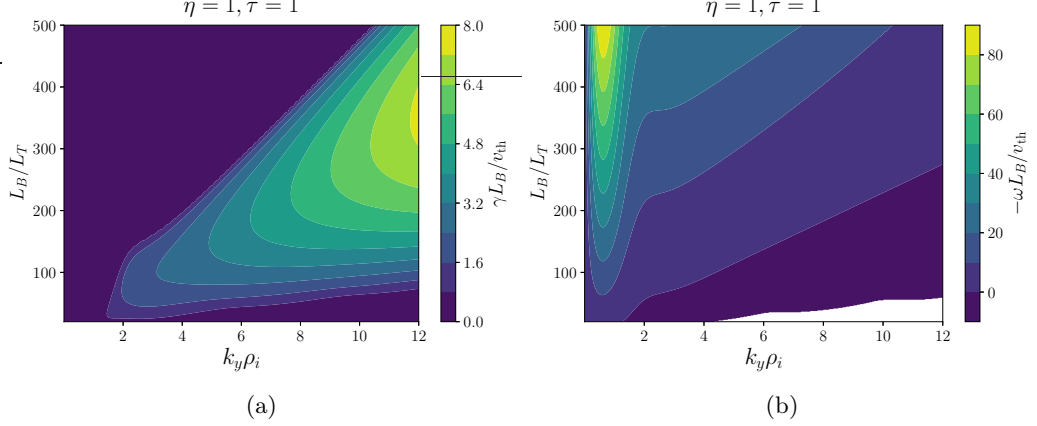


Figure 4: 2-D scan in L_B/L_T and $k_y\rho_i$ of the (a) growth rate and (b) real frequency obtained with the solver for $\tau = \eta = 1$. We note that the cutoff wave numbers where the growth rates pass through zero increase with L_B/L_T . Note that we plot the negative of the real frequencies here, so that the modes are propagating in the electron diamagnetic direction in contrast to the $\eta \rightarrow \infty$ case shown in Fig. 2.

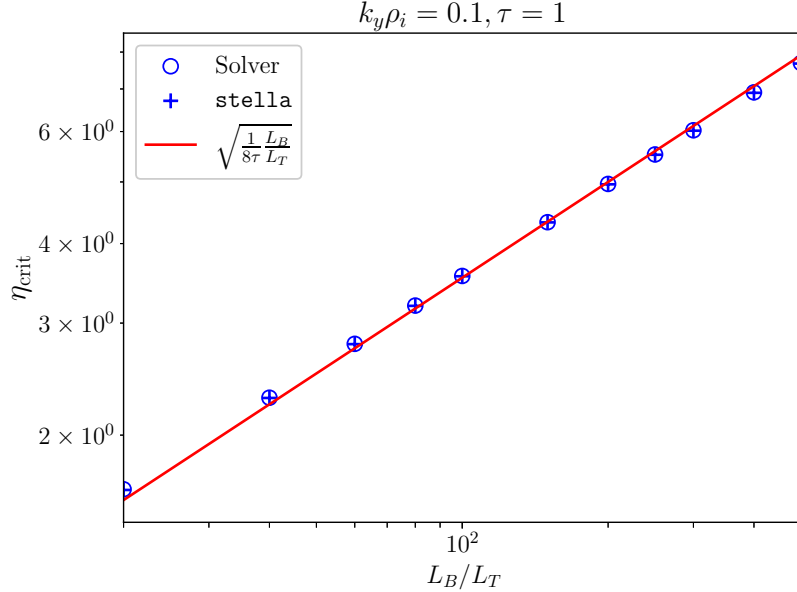


Figure 5: Plot of η_{crit} against L_B/L_T obtained from the semi-analytical solver (blue circles), the gyrokinetic code **stella**, (blue crosses), and the analytical prediction of Eq. (3.11) at $k_y\rho_i = 0.1$.

for the short-wavelength mode to be unstable and that this cutoff wave number increases with L_B/L_T . We plot this cutoff wave number, $k_y^o\rho_i$, against L_B/L_T^{eff} (for $\tau = 1$) in Fig. 7. For relatively small values of L_B/L_T ($L_B/L_T \lesssim 10$), the cutoff wave number satisfies $k_y^o\rho_i \ll 1$ and increases rapidly with L_B/L_T . At moderate L_B/L_T values ($10 \lesssim L_B/L_T \lesssim 100$), $k_y^o\rho_i \sim 1$ and has an apparent power-law scaling of $k_y^o\rho_i \propto (L_B/L_T)^{1/3}$.

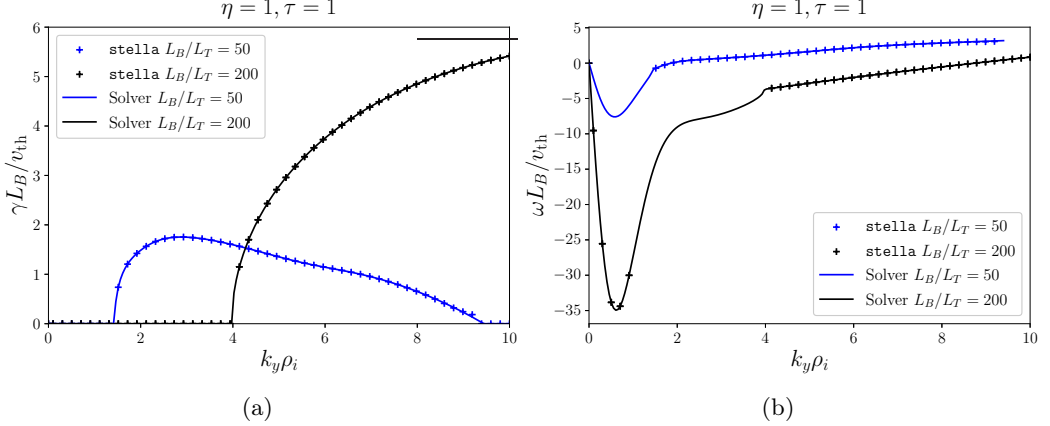


Figure 6: Plots of the (a) growth rate and (b) real frequency spectra for $L_B/L_T = 50$ and 200 with $\tau = \eta = 1$. As in the case where the density gradient is absent, we note that the cutoff wave number increases with L_B/L_T . The **stella** simulations used for this plot were run with 80 grid points in parallel velocity and 28 grid points in magnetic moment. No **stella** data points are plotted for the real frequency over part of the $k_y\rho_i$ range due to the difficulty in obtaining the frequency for damped modes.

As L_B/L_T increases further, $k_y^o\rho_i$ becomes large: in this asymptotic limit, $k_y^o\rho_i$ scales like L_B/L_T , consistent with the prediction of our heuristic fluid model developed in Sec. 3.2. In fact, the fluid model does a remarkably good job of predicting the variation of $k_y^o\rho_i$ with L_B/L_T across the full range of L_B/L_T considered, albeit with an approximately constant offset in L_B/L_T . This is despite the mode satisfying the condition $\omega \sim \omega_d$, which is inconsistent with the assumption $\omega \gg \omega_d$ underlying the fluid model.

In the limit of large L_B/L_T , the term proportional to ω in the numerator of the gyrokinetic dispersion Eq. relation (4.2) is small. The scaling of $k_y^o\rho_i$ with L_B/L_T^{eff} , the effective temperature gradient defined below Eq. (3.17), is then the same (up to a re-scaling) as that given for L_B/L_T . Extracting the τ dependence indicates that, at a fixed L_B/L_T , $k_y^o\rho_i$ should scale as $(1 + \tau)^{-1}$ for small τ and as $(1 + \tau)^{-1/3}$ for $\tau \sim 1$. This is confirmed in Fig. 7. A plot of the variation of the growth rate spectra with τ can be found in Appendix B.

Before exploring the implications of the k_y^o scalings for SWITG-driven turbulence, we assess the role played by the radial wave number k_x . Examining the gyrokinetic dispersion relation Eq. (4.2), one can see that the solution for ω/k_y must be isotropic in the (k_x, k_y) plane. This is because the only other appearance of k_x and k_y in the dispersion relation is via the k_\perp that appears in the argument of the Bessel function J_0 . We demonstrate this isotropy in Figure 8, where we plot $(\gamma L_B/v_{\text{th}})(2/k_y\rho_i)$ in the (k_x, k_y) plane for $\eta = \tau = 1$. Note that the instability peaks at $k_x = 0$, but it is possible for the system to be unstable even for $k_x < k_y^o$ when we allow k_x to be non-zero. However, as expected from the isotropy of γ/k_y , there appears to be a circular region of $k_\perp\rho_i \lesssim 1$ where the system is always stable.

5. Implications for turbulence

We have seen in Sec. 4 that the SWITG instability has a wavenumber cutoff that increases as the ion temperature gradient increases. If η is large enough for the long-

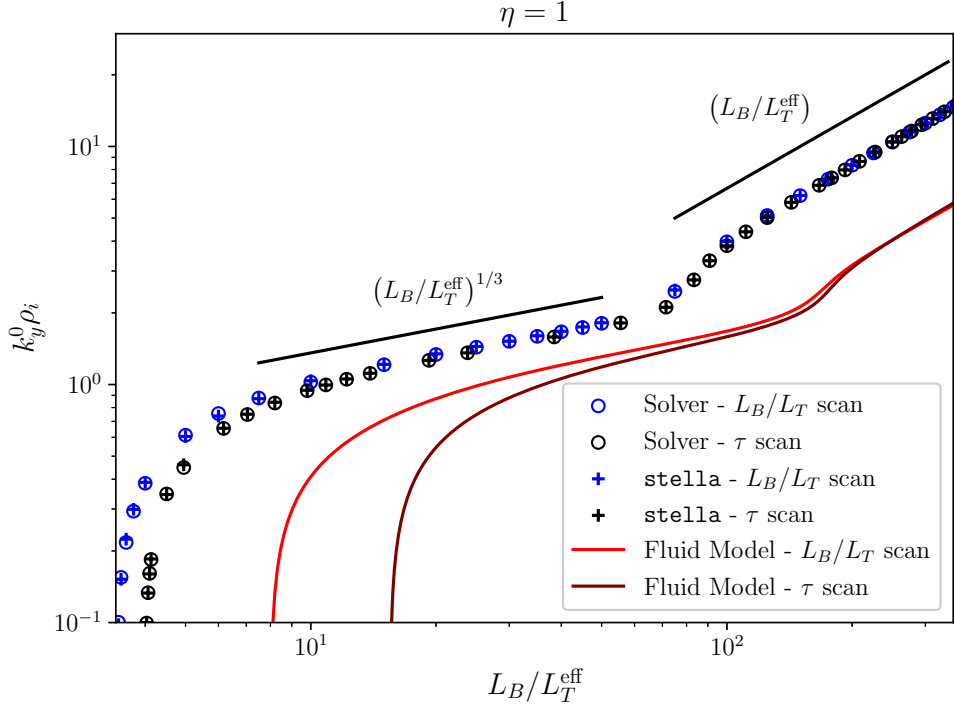


Figure 7: Plot of the cutoff wave number $k_y^0 \rho_i$ against L_B/L_T^{eff} at $\eta = 1$, obtained from the semi-analytical solver (circles), the gyrokinetic code **stella** (crosses), and the heuristic fluid model from Sec. 3.2 (red lines). Blue markers represent data obtained through a scan in L_B/L_T at $\tau = 1$ where $L_B/L_T \in [6.9, 700]$, and black markers represent data obtained through a scan in τ at $L_B/L_T = 500$ where $\tau \in [0.4, 123]$. We identify three distinct regimes: the drift kinetic limit for $k_y^0 \rho_i \ll 1$; the intermediate regime around $k_y^0 \rho_i \sim 1$, where the cutoff wave number scales as the power law $(L_B/L_T^{\text{eff}})^{1/3}$; and the $k_y^0 \rho_i \gg 1$ limit, where k_y^0 scales as L_B/L_T^{eff} . Note that the fluid results for both scans asymptote to the prediction in Eq. 3.17.

wavelength ITG to be destabilised, then the turbulence driven by the SWITG is unlikely to contribute significantly to transport: Large eddies are more effective at mixing than small eddies. However, if η is small enough for the long-wavelength ITG to be stabilised, then SWITG-driven transport could become important. A possible implication for the nonlinear dynamics associated with SWITG modes is that the outer scale of the turbulence will shift to shorter wavelengths as the driving gradients increase. To see the ramifications for transport, we adopt a simple diffusive estimate for the heat flux, with the diffusion coefficient χ estimated as

$$\chi \sim \frac{1}{(k_{\perp}^0)^2 \tau_{\text{nl}}^0}. \quad (5.1)$$

Here, τ_{nl}^0 is a measure of the characteristic nonlinear decorrelation time at the outer scale, and we have taken the characteristic radial extent of an eddy at the outer scale to be of size $1/k_{\perp}^0$, with k_{\perp}^0 the cutoff wavenumber for the linear SWITG mode. Note in this estimate that we have assumed $k_x^0 \sim k_{\perp}^0$. For the remainder of this section the superscript ‘o’ indicates a quantity evaluated at the outer scale.

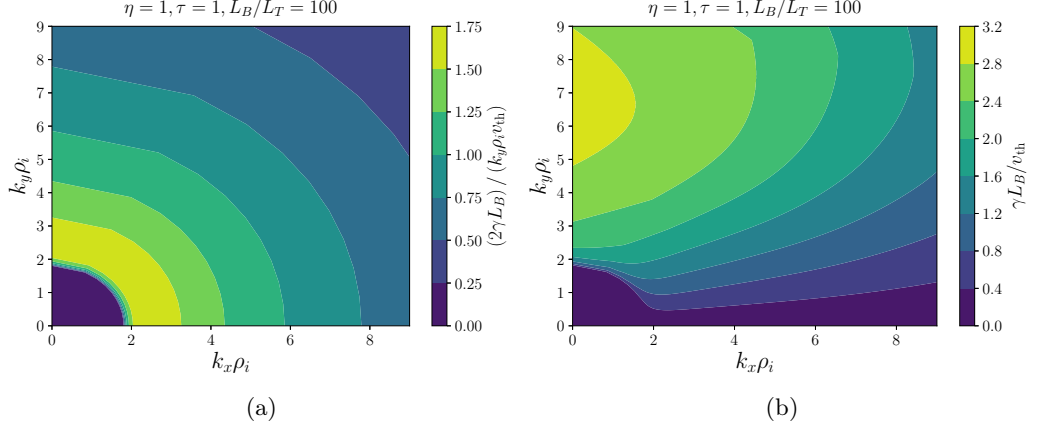


Figure 8: 2-D spectral plots of the growth rate produced using the solver for $L_B/L_T = 100$ and $\eta = \tau = 1$. Plot (a) is isotropic due to the presence of a normalisation factor proportional to k_y , while plot (b) omits the k_y in its normalisation.

We estimate the nonlinear decorrelation time at the outer scale by balancing the linear injection with the nonlinear transfer to smaller scales. To see how this works, first note from quasineutrality (2.12) that $\int d^3v J_0(\alpha_k) \hat{h}_k \sim (e\hat{\varphi}_k/T)n$, where we assume for simplicity that $T \equiv T_i = T_e$. Taking the velocity moment of the gyrokinetic equation (2.9) with the nonlinear term included then gives

$$\frac{\partial}{\partial t} \int d^3v J_0(\alpha_k) \hat{h}_k^o \sim \left(\int d^3v \langle \mathbf{v}_E \rangle_{\mathbf{R}} \cdot \nabla h \right)_{\mathbf{k}^o} \equiv \frac{e\hat{\varphi}_k^o}{T} \frac{n_i}{\tau_{\text{nl}}^o}, \quad (5.2)$$

where the middle term is the Fourier component of the $E \times B$ nonlinearity corresponding to the outer scale wave vector \mathbf{k}^o . Balancing this nonlinear transfer term with the linear drive finally yields

$$\frac{e\hat{\varphi}_k^o}{T} \frac{n_i}{\tau_{\text{nl}}^o} \sim \Gamma_0(b_k^o) \omega_*^o \eta \frac{e\hat{\varphi}_k^o}{T} n_i, \quad (5.3)$$

from which we obtain $\tau_{\text{nl}}^o \sim 1/(\Gamma_0(b_k^o) \omega_*^o \eta)$. The diffusivity then scales as

$$\chi \sim \frac{v_{\text{th}}}{L_T} \frac{\Gamma_0(b_k^o)}{k_{\perp}^o}. \quad (5.4)$$

When L_B/L_T is very large, $k_{\perp}^o \rho_i \gg 1$ so that $\Gamma_0(b_k^o) \sim 1/(k_{\perp}^o \rho_i)$ and the asymptotic scaling of Eq. (3.17) should be valid. In this limit, the diffusivity should *decrease* with increasing temperature gradient: $\chi \propto L_T$. This corresponds to an ion heat flux that is independent of ion temperature gradient. For the intermediate range of L_B/L_T values shown in Fig. 7, $k_{\perp}^o \propto L_T^{-1/3}$, but Γ_0 does not have a clear asymptotic scaling. Consequently, no power-law scaling for χ can be inferred in this non-asymptotic regime, though the empirical scaling for k_{\perp}^o suggests a weak (positive) scaling of χ with L_T^{-1} .

The SWITG instability we have considered is two-dimensional, but the turbulence it drives is unlikely to be. For two different planes perpendicular to the magnetic field to remain correlated, information must propagate between them. This provides a lower bound on the allowed k_{\parallel} for turbulent structures. The critical balance conjecture (Goldreich & Sridhar 1995; Barnes *et al.* 2011; Adkins *et al.* 2022; Nies *et al.* 2025; Adkins *et al.* 2026) provides a means of determining k_{\parallel} : The parallel correlation length of the turbulence is the distance that information can propagate before it is decorrelated

by the turbulent dynamics in the plane perpendicular to the magnetic field. In our case, the waves of interest are sound waves, and critical balance implies $k_{\parallel}v_{\text{th}} \sim \tau_{\text{nl}}^{-1}$. Using the above expression for τ_{nl}^o gives a scaling for the parallel outer scale with ion temperature gradient:

$$k_{\parallel}^o \sim \frac{1}{L_T}. \quad (5.5)$$

Thus, we anticipate that turbulent eddies driven by the SWITG mode have characteristic wavelengths both along and across the magnetic field that decrease with increasing temperature gradient. The aspect ratio of the eddies at the outer scale, $\epsilon^o \equiv k_{\perp}^o/k_{\parallel}^o$, is predicted to decrease with increasing temperature gradient as $\epsilon^o \sim L_T^{2/3}$ until very large L_B/L_T , when ϵ^o should become independent of L_T .

6. Discussion

In this paper we have considered the linear properties of the short-wavelength ITG (SWITG) instability for plasma consisting of a single ion species and Boltzmann electrons immersed in a constant-curvature magnetic field. When the ratio of the ion density gradient and temperature gradient scale lengths, η , is sufficiently small (cf. (3.11) and Fig. 5), the long-wavelength branch of the curvature ITG mode is stabilised. However, the SWITG mode remains unstable. We have shown that, unlike its long-wavelength counterpart, the SWITG has a cutoff wavenumber that *increases* with increasing temperature gradient: It follows the power-law scalings observed in Fig. 7 and predicted (at large temperature gradient) by Eq. (3.17). An immediate, counter-intuitive implication is that the linear growth rate of the SWITG mode at any fixed wavenumber will eventually decrease to zero as the temperature gradient increases, as illustrated in Fig. 4.

We showed in Sec. 5 that a simple diffusive estimate for the fluxes leads to scaling-law predictions for the ion heat flux and turbulence spatial and temporal scales associated with SWITG turbulence. Adoption of the critical balance conjecture further provides scalings for the parallel extent of turbulent eddies. For moderate values of the ion temperature gradient ($L_B/L_T \sim 10$), the parallel turbulence scale is predicted to decrease with increasing L_B/L_T faster than the perpendicular scale, and the ion heat flux Q is predicted to scale weakly with ion temperature gradient as $Q \propto (L_B/L_T)^{2/3}$. For large values of the ion temperature gradient ($L_B/L_T \gtrsim 100$), both the parallel and perpendicular turbulence outer scales are predicted to be inversely proportional to L_B/L_T , and the ion heat flux is predicted to be independent of the ion temperature gradient.

It should be emphasised that the analysis we have performed is limited in a variety of ways. Perhaps the most severe assumption we have made is that of a Boltzmann response for the electrons, which removes kinetic electron effects and electron-driven instabilities that can coexist with – and thus modify – the SWITG mode (cf. Chowdhury *et al.* (2009)). The use of a constant-curvature field removes particle trapping, magnetic shear and other physics associated with the variation of the magnetic field strength along a field line – each of which has been found to quantitatively modify SWITG mode growth rates (Gao *et al.* 2005; Chowdhury *et al.* 2009). We have ignored electromagnetic effects (Gao *et al.* 2005; Jagannath *et al.* 2020), radial profile shearing (Chowdhury *et al.* 2009) and numerous other factors that would be present in a realistic tokamak or stellarator plasma. The aim of our heuristic analysis is to give an indication of how the SWITG instability and associated turbulence properties should behave as the plasma density and temperature gradients are varied. A natural next step is to check the scaling-

law predictions provided here using nonlinear gyrokinetic simulations in both constant-curvature and more realistic tokamak or stellarator geometries, which we leave to a future publication.

Acknowledgements

This work was supported by the Engineering and Physical Sciences Research Council (EPSRC) [EP/R034737/1]. The authors would like to thank P. Luhadiya for helpful discussions regarding the semi-analytical solver described in this work.

Appendix A. Construction of the FLR solver

We adopt the notation used in [Ivanov & Adkins \(2023\)](#) and follow the prescription described in their §7 to solve the resonant integral in equation (4.2) numerically while incorporating FLR effects.

Equation (4.2) can be expressed in the form

$$1 + \tau + \left[\omega - \omega_* + \eta \omega_* \left(\partial_s + \partial_t + \frac{3}{2} \right) \mathcal{I}_{s,t} \Big|_{s=t=1} \right] = 0, \quad (\text{A } 1)$$

where[†]

$$\mathcal{I}_{s,t} = \frac{1}{\sqrt{\pi}} \int_{-\infty}^{\infty} du \int_0^{\infty} d\mu \frac{e^{-su^2-t\mu}}{-\omega + \omega_d(2u^2 + \mu)} J_0^2(\alpha_k). \quad (\text{A } 2)$$

The factor of $J_0^2(x)$ appearing in (A 2) can be represented as a convergent power series ([Watson 1922](#)) such that

$$J_0^2(\alpha_k) = \sum_{m=0}^{\infty} \frac{(-1)^m (2m)!}{(m!)^4} \left(\frac{\alpha_k}{2} \right)^{2m}, \quad (\text{A } 3)$$

where $\alpha_k^2 = \mu(k_{\perp} \rho_i)^2$. We thus have

$$\mathcal{I}_{s,t} = \sum_{m=0}^{\infty} \frac{(2m)!}{(m!)^4} b_k^m \partial_t^m I_{s,t}, \quad (\text{A } 4)$$

where $b_k \equiv (k_{\perp} \rho_i)^2 / 2$, and $I_{s,t}$ is the resonant integral in the drift-kinetic limit, i.e.,

$$I_{s,t} = \frac{1}{\sqrt{\pi}} \int_{-\infty}^{\infty} du \int_0^{\infty} d\mu \frac{e^{-su^2-t\mu}}{-\omega + \omega_d(2u^2 + \mu)}. \quad (\text{A } 5)$$

From (A 5), we see that $I_{1,1}$ is the same as equation (4.2) in the drift-kinetic limit and can be expressed in terms of the plasma dispersion function ([Biglari et al. 1989; Zocco et al. 2018](#)) as

$$I_{1,1} = -\frac{1}{2\omega_d} Z^2(\sqrt{\hat{\omega}}), \quad \hat{\omega} = \frac{\omega}{2\omega_d}. \quad (\text{A } 6)$$

The plasma dispersion function ([Fried & Conte 1961](#)) is defined to be

$$Z(x) = \frac{1}{\sqrt{\pi}} \int_{-\infty}^{\infty} dy \frac{e^{-y^2}}{y - x}. \quad (\text{A } 7)$$

[Ivanov & Adkins \(2023\)](#) also provide analytical expressions for the derivatives of $I_{s,t}$

[†] Note that $\mathcal{I}_{s,t}$ as defined here is the 2-D simplification ($k_{\parallel} v_{\text{th}} \rightarrow 0$) of $\mathcal{I}_{s,t}$ as defined in [Ivanov & Adkins \(2023\)](#).

in terms of $I_{s,t}$. Hence, if the m^{th} derivative of $I_{s,t}$ can be determined recursively in terms of $I_{s,t}$ and then evaluated at $s = t = 1$, we can subsequently solve equation (4.2) numerically. This cannot be done in general but is possible for the 2-D case that we are concerned with. This is what we will now describe.

The derivative of $I_{s,t}$, derived in Appendix B of [Ivanov & Adkins \(2023\)](#), is

$$\partial_t I_{s,t} = \frac{1}{s-2t} \left[I_{s,t}(-2\hat{\omega}(s-2t)+1) - \frac{2}{\omega_d} \sqrt{\hat{\omega}} Z_s(\sqrt{\hat{\omega}}) - \frac{\sqrt{s}}{t\omega_d} \right], \quad (\text{A } 8)$$

where $Z_s(x) = Z(\sqrt{s}x)$. Generalisation to the m^{th} derivative gives

$$\begin{aligned} \partial_t^m I_{s,t} = & \frac{1}{s-2t} \left[(2m-1-2\hat{\omega}(s-2t)) \partial_t^{m-1} I_{s,t} \right. \\ & \left. + 4\hat{\omega}(m-1) \partial_t^{m-2} I_{s,t} + \left(\frac{-1}{t} \right)^m \frac{\sqrt{s}}{\omega_d} (m-1)! \right]. \end{aligned} \quad (\text{A } 9)$$

Setting $s = t = 1$ allows us to compute the power series in equation (A 4). To compute $(\partial_s + \partial_t) \partial_t^m I_{s,t}$, we note that $(\partial_s + \partial_t) f(s, t)|_{t=s} = \partial_s f(s, t = s)$.

Hence, we set $t = s$ in equation (A 9) and differentiate with respect to s :

$$\begin{aligned} \partial_s (\partial_t^m I_{s,t}|_{t=s}) = & \frac{-1}{s} \left[\partial_t^m I_{s,t}|_{t=s} + 2\hat{\omega} \partial_t^{m-1} I_{s,t}|_{t=s} + (2m-1+2\hat{\omega}s) \partial_s (\partial_t^{m-1} I_{s,t}|_{t=s}) \right. \\ & \left. + 4\hat{\omega}(m-1) \partial_s (\partial_t^{m-2} I_{s,t}|_{t=s}) + \frac{(-1)^{m+1}}{s^{m+1/2} \omega_d} (m-1)! \left(m - \frac{1}{2} \right) \right]. \end{aligned} \quad (\text{A } 10)$$

When evaluated at $s = t = 1$, equations (A 9) and (A 10) represent the recursion relations that allow us to solve (4.2) numerically. Closure of the recursive process requires explicit specification of the left-hand sides of equations (A 9) and (A 10) for $m = 0$ and $m = 1$. For (A 9), these quantities are

$$I_{1,1} = -\frac{1}{2\omega_d} Z^2(\sqrt{\hat{\omega}}) \quad \partial_t I_{s,t}|_{t=s=1} = \frac{1}{2\omega_d} \left[Z^2(\sqrt{\hat{\omega}})(1+2\hat{\omega}) + 4\sqrt{\hat{\omega}} Z(\hat{\omega}) + 2 \right], \quad (\text{A } 11)$$

and for equation (A 10),

$$\begin{aligned} \partial_s I_{s,s}|_{s=1} = & \frac{1}{4\omega_d} Z^2(\sqrt{\hat{\omega}}) + \frac{1}{\omega_d} \sqrt{\hat{\omega}} Z(\sqrt{\hat{\omega}}) \left[1 + \sqrt{\hat{\omega}} Z(\sqrt{\hat{\omega}}) \right], \\ \partial_s (\partial_t I_{s,t}|_{t=s})|_{s=1} = & -\partial_s I_{s,s}|_{s=1} (2\hat{\omega}+1) + \frac{1}{2\omega_d} Z^2(\sqrt{\hat{\omega}}) - \frac{2}{\omega_d} \sqrt{\hat{\omega}} Z(\sqrt{\hat{\omega}}) \\ & - \frac{2}{\omega_d} \hat{\omega} \left[1 + \sqrt{\hat{\omega}} Z(\sqrt{\hat{\omega}}) \right] - \frac{3}{2\omega_d}. \end{aligned} \quad (\text{A } 12)$$

Using these recursion relations and a quick numerical implementation of the plasma dispersion function such as from [Johnson \(2015\)](#), one can solve the linearised gyrokinetic equation (4.2) to arbitrarily high $k_{\perp}\rho_i$ using a root finding algorithm. This is provided that one uses enough terms in the expansion for the Bessel function such that the expansion is a sufficiently good approximation to the actual value at a given $k_{\perp}\rho_i$. The number of terms required increases rapidly with the value of $k_{\perp}\rho_i$. We used $m = 60$ for $k_{\perp}\rho_i = 6$, $m = 150$ for $k_{\perp}\rho_i = 8$ (cf. Fig. 3), $m = 250$ for $k_{\perp}\rho_i = 10$ (cf. Fig. 6), $m = 450$ for $k_{\perp}\rho_i = 12$ (cf. Fig. 2), and $m = 650$ for $k_{\perp}\rho_i = 13$ (cf. Fig. 8).

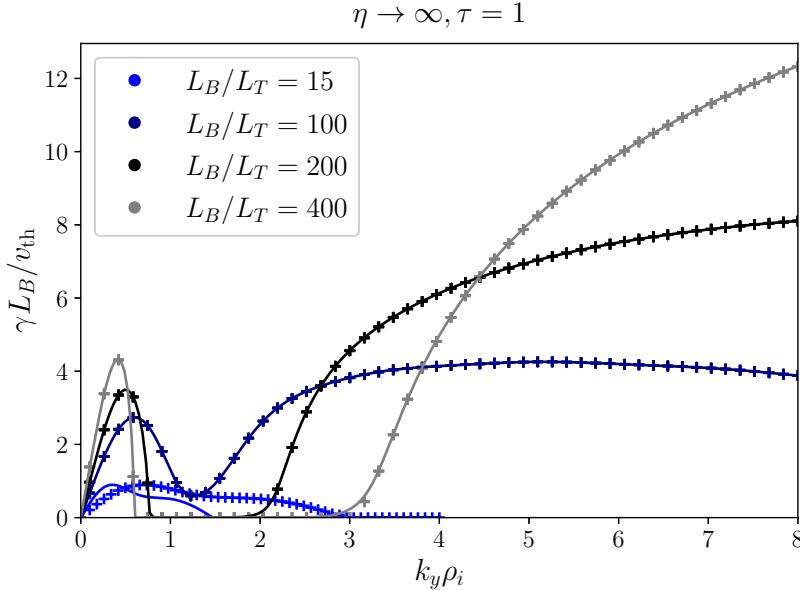


Figure 9: Plots of the growth rate spectra made using **stella** (crosses) and the semi-analytical solver (lines) with $\eta \rightarrow \infty$ and $L_B/L_T = 15, 100, 200$, and 400 .

Appendix B. Additional growth rate spectra

Here, we present additional 1D cuts of the growth rate spectra discussed in Section 4, highlighting key features of the instability.

We first show in Figure 9 the growth rate spectra in the $\eta \rightarrow \infty$ limit for several different values of L_B/L_T . Note that the SWITG cutoff wavenumber increases with L_B/L_T : at large L_B/L_T values, the long-wavelength and short-wavelength ITG spectra are distinct, and they merge at more modest values of L_B/L_T , giving the characteristic double-bump structure seen in previous studies.

The variation of the growth rate spectrum with density gradient is illustrated in Figure 10. The data is taken from simulations with fixed $L_B/L_T = 200$, $\tau = 1$ and with η varying from 1.25 to 10. The main effect of an increasing density gradient is to stabilise the long-wavelength ITG, leading to a clear cutoff at long-wavelengths for the SWITG. There is also a modest, non-monotonic modification to the SWITG growth rates.

Finally, the effect of varying the ion-electron temperature ratio τ is captured in Figure 11, in which the growth rate spectra are plotted for fixed $\eta = 1$, $L_B/L_T = 100$ and τ varying from 0.1 to 3. The cutoff wavenumber for the SWITG increases as τ decreases, in line with the predictions of the heuristic fluid model presented in Section 3.

REFERENCES

ABEL, I. G., PLUNK, G. G., WANG, E., BARNES, M., COWLEY, S. C., DORLAND, W. & SCHEKOCHIHIHIN, A. A. 2013 Multiscale gyrokinetics for rotating tokamak plasmas: fluctuations, transport and energy flows. *Reports on Progress in Physics* **76** (11), 116201.

ABRAMOWITZ, MILTON & STEGUN, IRENE A. 1968 *Handbook of mathematical functions with formulas, graphs, and mathematical tables*, , vol. 55. US Government printing office.

ADKINS, T., ABEL, I. G., BARNES, M., BULLER, S., DORLAND, W., IVANOV, P. G.,

$$L_B/L_T = 200, \tau = 1$$

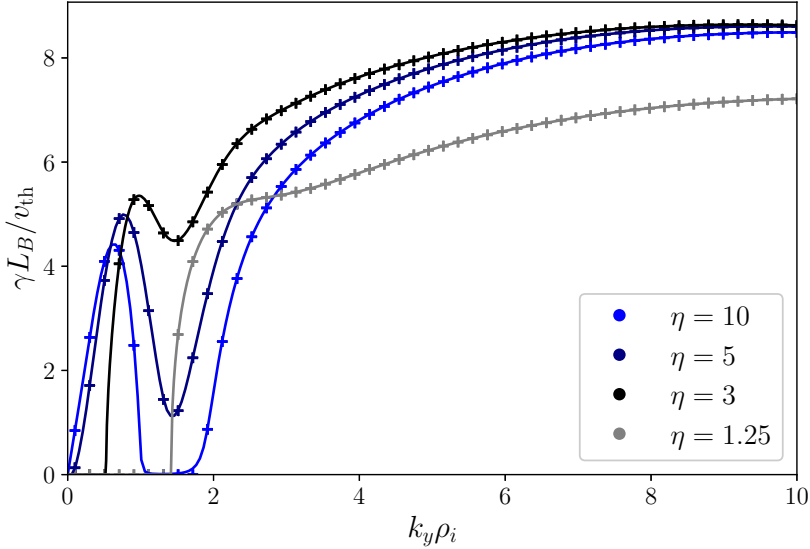


Figure 10: Plots of the growth rate spectra made using **stella** (crosses) and the semi-analytical solver (lines) for different values of the density gradient at fixed $L_B/L_T = 200$, $\tau = 1$.

$$L_B/L_T = 100, \eta = 1$$

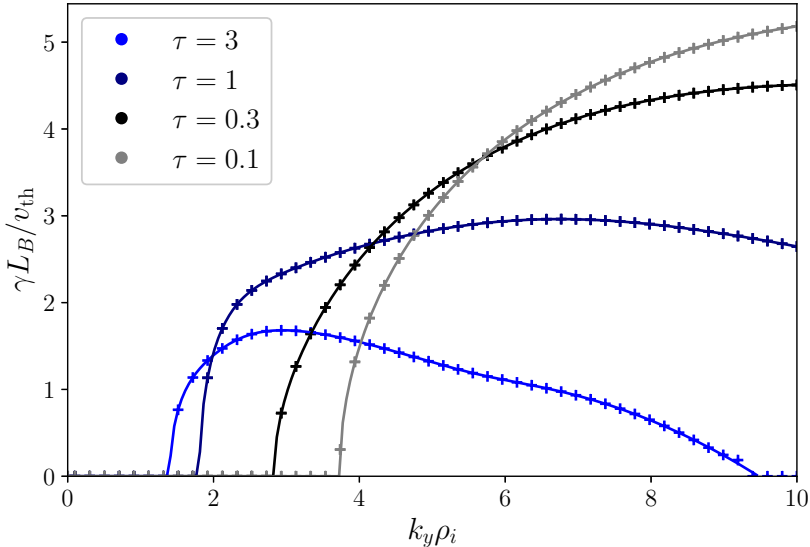


Figure 11: Plots of the growth rate spectra made using **stella** (crosses) and the semi-analytical solver (lines) for $L_B/L_T = 100$, $\eta = 1$, and $\tau = 3, 1, 0.3$, and 0.1 . Decreasing τ has a similar effect to increasing L_B/L_T ; i.e., the cutoff wavenumber of the instability is pushed to larger values.

MEYRAND, R., PARRA, F. I., SCHEKOCHIHIHIN, A. A. & SQUIRE, J. 2026 Asymptotic scaling theory of electrostatic turbulent transport in magnetised fusion plasmas , arXiv: 2601.15391.

ADKINS, T., SCHEKOCHIHIHIN, A. A., IVANOV, P. G. & ROACH, C. M. 2022 Electromagnetic instabilities and plasma turbulence driven by electron-temperature gradient. *Journal of Plasma Physics* **88** (4), 905880410.

BARNES, MICHAEL, PARRA, FELIX I. & LANDREMAN, MATT 2019 stella: An operator-split, implicit-explicit δf -gyrokinetic code for general magnetic field configurations. *Journal of Computational Physics* **391**, 365–380.

BARNES, M., PARRA, F. I. & SCHEKOCHIHIHIN, A. A. 2011 Critically balanced ion temperature gradient turbulence in fusion plasmas. *Physical Review Letters* **107** (11), 115003.

BIGLARI, H., DIAMOND, P. H. & ROSENBLUTH, M. N. 1989 Toroidal ion-pressure-gradient-driven drift instabilities and transport revisited. *Physics of Fluids B* **1** (1), 109–118.

BOZHENKOV, S. A., KAZAKOV, Y., FORD, O. P., BEURSKENS, M. N. A., ALCUSÓN, J., ALONSO, J. A., BALDZUHN, J., BRANDT, C., BRUNNER, K. J., DAMM, H., FUCHERT, G., GEIGER, J., GRULKE, O., HIRSCH, M., HÖFEL, U., HUANG, Z., KNAUER, J., KRYCHOWIAK, M., LANGENBERG, A., LAQUA, H. P., LAZERSON, S., MARUSHCHENKO, N. B., MOSEEV, D., OTTE, M., PABLANT, N., PASCH, E., PAVONE, A., PROLL, J. H. E., RAHBARNIA, K., SCOTT, E. R., SMITH, H. M., STANGE, T., VON STECHOW, A., THOMSEN, H., TURKIN, YU., WURDEN, G., XANTHOPOULOS, P., ZHANG, D., WOLF, R. C. & THE W7-X TEAM 2020 High-performance plasmas after pellet injections in wendelstein 7-x. *Nuclear Fusion* **60** (6), 066011.

CHOWDHURY, J., BRUNNER, S., GANESH, R., LAPILLONNE, X., VILLARD, L. & JENKO, F. 2012 Short wavelength ion temperature gradient turbulence. *Physics of Plasmas* **19**, 102508.

CHOWDHURY, J., GANESH, R., VACLAVIK, J., BRUNNER, S., VILLARD, L. & ANGELINO, P. 2009 Short wavelength ion temperature gradient mode and coupling with trapped electrons. *Physics of Plasmas* **16**, 082511.

EVENSEN, H. T., FONCK, R. J., PAUL, S. F., REWOLDT, G., SCOTT, S. D., TANG, W. M. & ZARNSTORFF, M. C. 1998 Measurements of ion temperature fluctuations in the tokamak fusion test reactor. *Nuclear Fusion* **38**, 237.

FRIED, BURTON D. & CONTE, SAMUEL D. 1961 The plasma dispersion function .

FRIEMAN, E. A. & CHEN, LIU 1982 Nonlinear gyrokinetic equations for low-frequency electromagnetic waves in general plasma equilibria. *The Physics of Fluids* **25** (3), 502–508.

GAO, ZHE, SANUKI, H., ITOH, K. & DONG, J. Q. 2003 Temperature gradient driven short wavelength modes in sheared slab plasmas. *Physics of Plasmas* **10** (7), 2831–2839.

GAO, ZHE, SANUKI, H., ITOH, K. & DONG, J. Q. 2005 Short wavelength ion temperature gradient instability in toroidal plasmas. *Physics of Plasmas* **12** (2), 022502.

GAO, ZHE, SANUKI, H., ITOH, K. & DONG, J. Q. 2006 Critical gradients for short wavelength ion temperature gradient instability in toroidal plasmas. *Journal of Plasma Physics* **72** (6), 1249–1252.

GOLDRICH, P. & SRIDHAR, S. 1995 Toward a theory of interstellar turbulence. ii. strong alfvénic turbulence. *The Astrophysical Journal* **438**, 763.

GUO, S. C. & ROMANELLI, F. 1993 The linear threshold of the ion-temperature-gradient-driven mode. *Physics of Fluids B* **5** (2), 520–533.

GUZDAR, P. N., CHEN, LIU, TANG, W. M. & RUTHERFORD, P. H. 1983 Ion-temperature-gradient instability in toroidal plasmas. *Physics of Fluids* **26** (3), 673–677.

HASSAM, A. B., T. M. ANTONSEN, JR., DRAKE, J. F. & GUZDAR, P. N. 1990 Theory of ion temperature gradient instabilities: Thresholds and transport. *Physics of Fluids B* **2** (8), 1822–1832.

HIROSE, AKIRA, ELIA, M., SMOLYAKOV, A. I. & YAGI, M. 2002 Short wavelength temperature gradient driven modes in tokamaks. *Physics of Plasmas* **9** (5), 1659–1666.

HORTON, W., CHOI, D. I. & TANG, W. M. 1981 Toroidal drift modes driven by ion pressure gradients. *Physics of Fluids* **24**, 1077.

IVANOV, P. G. & ADKINS, T. 2023 An analytical form of the dispersion function for local linear gyrokinetics in a curved magnetic field. *Journal of Plasma Physics* **89** (2), 905890213.

JAGANNATH, M., CHOWDHURY, J., GANESH, R. & VILLARD, L. 2020 Finite

beta effects on short wavelength ion temperature gradient modes. *Physics of Plasmas* **27** (5), 052509.

JOHNSON, STEVEN G. 2015 Faddeeva package.

NIES, R., PARRA, F. I., BARNES, M., MANDELL, N. & DORLAND, W. 2025 Saturation of magnetised plasma turbulence by propagating zonal flows. *submitted to Physical Review Letters* ArXiv:2409.02283.

POGUTSE, O. P. 1968 Magnetic drift instability in a collisionless plasma. *Plasma Physics* **10** (7), 649–664.

PU, YI-KANG & MIGLIUOLO, STEFANO 1985 Finite beta stabilization of the kinetic ion mixing mode. *The Physics of Fluids* **28** (6), 1722–1726.

RODRÍGUEZ, E. & ZOCCO, A. 2025 The kinetic ion-temperature-gradient-driven instability and its localisation. *Journal of Plasma Physics* **91** (1), E21.

ROMANELLI, F. 1989 Ion temperature-gradient-driven modes and anomalous ion transport in tokamaks. *Physics of Fluids B* **1**, 1018–1025.

SINGH, AMIT K., MAHAPATRA, JAGANNATH, CHOWDHURY, JUGAL, AGGARWAL, D., GANESH, R., HAYWARD-SCHNEIDER, T., LANTI, E., MISHCHENKO, A., McMILLAN, B. G. & VILLARD, L. 2023 Gyrokinetic simulation of short wavelength ion temperature gradient instabilities in the aditya-u tokamak. *Nuclear Fusion* **63** (8), 086029.

SMOLYAKOV, A. I., YAGI, M. & KISHIMOTO, Y. 2002 Short wavelength temperature gradient driven modes in tokamak plasmas. *Physical Review Letters* **89** (12), 125005.

SUGAMA, H. & HORTON, W. 1997 Transport processes and entropy production in toroidally rotating plasmas with electrostatic turbulence. *Physics of Plasmas* **4** (2), 405–418.

TERRY, P., ANDERSON, W. & HORTON, W. 1982 Kinetic effects on the toroidal ion pressure gradient drift mode. *Nuclear Fusion* **22** (4), 487.

THOMAS M. ANTONSEN, JR. & LANE, BARTON 1980 Kinetic equations for low frequency instabilities in inhomogeneous plasmas. *The Physics of Fluids* **23** (6), 1205–1214.

WATSON, GEORGE NEVILLE 1922 *A treatise on the theory of Bessel functions*, , vol. 2. The University Press.

YOSHIDA, M., McDERMOTT, R. M., ANGIONI, C., CAMENEN, Y., CITRIN, J., JAKUBOWSKI, M., HUGHES, J. W., IDOMURA, Y., MANTICA, P., MARIANI, A., MORDJCK, S., PAUL, E. J., TALA, T., VERDOOLAEGE, G., ZOCCO, A., CASSON, F. J., DIF-PRADALIER, G., DUVAL, B., GRIERSON, B., KAYE, S. M., MANAS, P., MASLOV, M., ODSTRCIL, T., RICE, J. E., SCHMITZ, L., SCIORTINO, F., SOLANO, E. R., STAEBLER, G., VALOVIĆ, M., WOLFRUM, E., SNIPES, J. A., THE TRANSPORT & GROUP, CONFINEMENT 2025 Transport and confinement physics: Chapter 2 of the special issue: on the path to tokamak burning plasma operation. *Nuclear Fusion* **65** (3), 033001.

ZOCCO, A., XANTHOPOULOS, P., DOERK, H., CONNOR, J. W. & HELANDER, P. 2018 Threshold for the destabilisation of the ion-temperature-gradient mode in magnetically confined toroidal plasmas. *Journal of Plasma Physics* **84** (1), 715840101.